Proceedings of the Thirty-fifth (2025) International Ocean and Polar Engineering Conference **www.isope.org**
Seoul/Goyang, Korea, June 1-6, 2025

ISBN 978-1-880653-74-6; ISSN 1098-6189

Impact of Tandem on Flow Characteristics around Surface-piercing Finite Circular Cylinders

Minghai Wang[1], *Wenbin Zhang*[1], *Wentao Wang*[1,2], *Decheng Wan*[1]*

[1] Computational Marine Hydrodynamics Lab (CMHL), School of Naval Architecture, Ocean and Civil Engineering,
Shanghai Jiao Tong University, Shanghai, China
[2] China Ship Scientific Research Center, Wuxi, China
*Corresponding Author

ABSTRACT

Tandem surface-piercing finite circular cylinders are common structures in ocean and coastal engineering. This work presents high-fidelity numerical simulations of the flow past single and two tandem cylinders based on the adaptive mesh refinement technique. The free surface is captured using a geometrical volume of fluid method based on piecewise linear interface calculation. The Dirichlet boundary condition on the cylinders is archived using the embedded boundary method. The flow characteristics are compared to the flow field past a single cylinder and discussed. A parametric study investigates the distinct flow patterns depending on the gap/diameter ratio l/D between two cylinders. The distance is divided into three different cases: close ($l/D=2$), medium ($l/D=3$), and far ($l/D=5$). The free surface deformation, the velocity distribution, and the vortex shedding features are all influenced by the tandem arrangement. Moreover, the tandem arrangement together with the free surface and the free end shows combined effects on the flow field. This study contributes to applying adaptive mesh refinement technique on the flow-structure interaction and provides a valuable reference for ocean engineering applications.

KEY WORDS: adaptive mesh refinement; free surface; tandem cylinders; air entrainment;

INTRODUCTION

Surface-piercing cylinders are simplified models for many Marine engineering structures. A single surface-piercing cylinder can represent marine platforms including Spar, cylindrical FPSO, aquaculture cage, etc. The piles or mooring lines of a floating platform foundation, as well as a row of marine risers, can be simplified as tandem surface-piercing cylinders. Hence, understanding the behavior of the free surface as it interacts with the cylinders is an interesting endeavor with an increasing amount of interest (Keough et al., 2024).

Flow past a surface-piercing circular cylinder has been extensively studied through experiments and numerical simulations. In the early years, Hay (1947) conducted extensive experiments on flow past surface-piercing circular cylinders with various cylinder diameters, draught, and inlet velocities. Due to the limitations of measurement and photographic techniques, Hay's studies did not involve detailed characteristics in the free surface deformation and flow field. In recent years, owing to significant advancements in pool experiment technology and high-performance computer technology, numerous experimental studies (Ageorges et al., 2019; Chaplin and Teigen, 2003; Hilo et al., 2022; Keough et al., 2024) and numerical studies (Ageorges et al., 2021; Chen et al., 2022; Kawamura et al., 2001; Koo et al., 2014; Suh et al., 2011) have been conducted on the flow around a surface-piercing cylinder at various Froude numbers, Reynolds numbers and cylinder sizes. Detailed flow structures and the impact of the free surface on the cylinder flow have been thoroughly investigated. The free surface was found to dramatically change the drag force distribution in the spanwise of the cylinder and attenuate the vortex shedding. A large number of small flow structures were generated near the free surface and produced many unique flow phenomena. Among the studies, Chen et al. (2022) provided a thorough investigation of the turbulent structures and characteristics of flows past a vertical surface-piercing finite circular cylinder at $Fr=1.1$ and $Re=2.7\times10^5$ recently. The effects of the free surface and the free end, the velocity profile, separation angle, vorticity, and turbulent kinematic energy at different spanwise positions were discussed respectively. The instantaneous and time-averaged primary vortex structures were identified and examined by using the Omega-Liutex method. A spectral analysis at different probes on the cylinder surface and in the wake region determining the dominant frequencies for each primary turbulent structure was also included.

The introduction of tandem effects makes the problem more complex. For the single-phase flow, the tandem impact on the vortex shedding in the cylinder wake has been classified into three distinct flow regimes according to the gap/diameter ratio l/D by Zdravkovich, (1987). For $1<l/D<1.2\sim1.8$ depending on the Reynold number, the free shear layers separated from the upstream cylinder do not reattach on the downstream cylinder. The vortex street is actually formed by the free shear layers detached from the former. For $1.2\sim1.8<l/D<3.4\sim3.8$, the free shear layers reattach on the upstream side of downstream cylinder. A vortex street is formed only behind the downstream cylinder. For $l/D>3.4\sim3.8$, the separated shear layers roll up alternately and form vortices between the gap and two vortex streets are formed behind the cylinders. Similar flow regimes were also observed by numerical simulations at various Froude numbers and Reynold numbers (Carmo and Meneghini, 2006; Kitagawa and Ohta, 2008).

However, to the best of our knowledge, the flow past two tandem surface-piercing circular cylinders is rarely researched. The primary focus of this study is to fill in the gaps and study the interaction between the tandem impact and the free surface. First of all, the numerical approaches used in this study are introduced. Then the numerical setup including the physical model, the computational domain and mesh, and a numerical validation is presented. The results and discussions focus on the tandem effect on the free surface, the vertical velocity distribution, and the vertical vorticity at different spanwise directions to investigate the three-dimensional flow features. Finally, the main conclusions are drawn.

NUMERICAL APPROACHES

Governing equations

The Navier-Stokes equation for the two-phase flow is solved in three dimensions using relevant solvers in *Basilisk* with surface tension considered. The governing equations are presented as follows:

$$\begin{cases} \rho\left[\dfrac{\partial \boldsymbol{u}}{\partial t}+\boldsymbol{u}(\nabla\cdot\boldsymbol{u})\right]=-\nabla p+\mu\nabla^2\boldsymbol{u}+\rho\boldsymbol{g}+\sigma\kappa\delta_s\boldsymbol{n} \\ \dfrac{\partial\rho}{\partial t}+\nabla\cdot(\rho\boldsymbol{u})=0 \end{cases} \tag{1}$$

where ρ is the density of fluid, $\boldsymbol{u}=(u,v)$ is the velocity vector of fluid, p is pressure, μ is the fluid dynamic viscosity. The term $\sigma\kappa\delta_s\boldsymbol{n}$ is introduced to consider the effect of surface tension where σ is the surface tension coefficient, κ and $\boldsymbol{n}$ are the curvature and normal unit vector to the interface, and the surface Dirac function δ_s helps distinguish the fluid interface. It equals one on the interface and zero otherwise.

In order to capture the free surface between the air phase and water phase, the volume of fluid method (VOF) is adopted. The fraction function $\alpha(\boldsymbol{x},t)$ is introduced as the volume fraction of water in each cell. The density and viscosity of a cell can be written as:

$$\begin{cases} \rho(\boldsymbol{x},t)=\alpha(\boldsymbol{x},t)\rho_w+(1-\alpha(\boldsymbol{x},t))\rho_a \\ \mu(\boldsymbol{x},t)=\alpha(\boldsymbol{x},t)\mu_w+(1-\alpha(\boldsymbol{x},t))\mu_a \end{cases} \tag{2}$$

where ρ_a, ρ_w, μ_a, μ_w are the density and viscosity of air and water. The evolution of the interface is given by the advection equation below:

$$\frac{\partial\alpha}{\partial t}+\nabla\cdot(\alpha\boldsymbol{u})=0 \tag{3}$$

Adaptive mesh refinement

As implemented in the *Basilisk* solver, the tree-based adaptive mesh refinement technique (AMR) plays a crucial role in enhancing the accuracy of numerical simulations while conserving computational resources. This method dynamically adjusts the mesh cell size throughout the simulation, allowing for a more detailed examination of small-scale flow structures such as bubbles and droplets, which are critical in this study.

The AMR module in *Basilisk* is powered by wavelet analysis, which is rooted in multi-resolution analysis and allows for estimating numerical errors in the representation of spatially discretized fields. This study uses the gradient of the velocity field and the volume fraction field for wavelet analysis. When the gradient of the velocity field or the volume fraction field of water reaches a predefined threshold of 0.01, the parent cell is refined into eight child cells. (shown in Fig. 1)

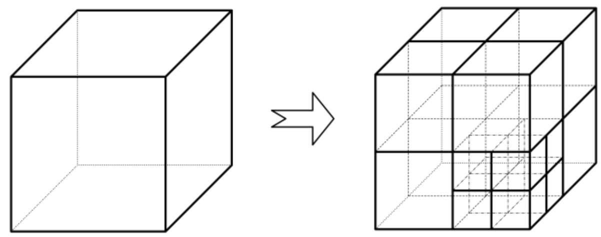

Fig. 1 Octree adaptive mesh refinement

Embedded boundary method

The Embedded boundary method, also known as the cut-cell method, is adopted to simulate the curved cylinder surface in adaptive Cartesian meshes. An approach similar to the PLIC method in VOF is employed to capture a sharp solid interface. First of all, a signed function $\phi(\boldsymbol{x})$ is applied to the vertexes of the cell (shown in Fig. 2(a)). Specify solids inside $\phi<0$, outside $\phi>0$. Then determine the line fraction λ_d on each boundary of the cell, representing the fraction of solids on that edge:

$$\lambda_d=\frac{1-sign(\phi_1)}{2}+sign(\phi_1)\frac{\phi_1}{\phi_1-\phi_2},\quad \phi_1\phi_2<0 \tag{4}$$

where d represents the sides, $sign$ represents the sign function, and ϕ_1, ϕ_2 is the value of any two vertices. From the line fractions on all boundaries, the interface normal $\boldsymbol{n}_S$ and solid volume fraction C_S can be calculated:

$$\boldsymbol{n}_s=-\left(\sum_d\lambda_d\boldsymbol{n}_d\right)\Big/\left|\sum_d\lambda_d\boldsymbol{n}_d\right| \tag{5}$$

$$C_S=F(\boldsymbol{n}_S,\lambda_d) \tag{6}$$

where, $\boldsymbol{n}_d$ is the normal direction of each boundary and F is a predefined function in *Basilisk*.

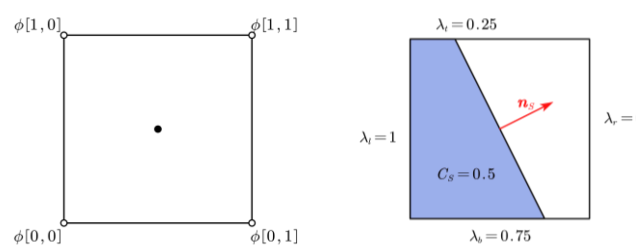

(a) (b)

Fig. 2 The calculation of the solid volume fraction

Then a 3-D implementation of variable values on the solid interface described by Schwartz et al. (2006) is used to achieve the Dirichlet boundary condition on the solid surface:

$$\frac{\partial \phi}{\partial \boldsymbol{n}} = \frac{1}{d_2 - d_1}\left[\frac{d_2}{d_1}(\phi^B - \phi_1^I) - \frac{d_1}{d_2}(\phi^B - \phi_2^I)\right] \tag{7}$$

where ϕ^B is the value of ϕ on the solid interface. . ϕ_1^I ., ϕ_2^I , are the values of ϕ on the two points for gradient interpolation, respectively. d_1 , d_2 are the distances between the solid interface and the two points. The values of ϕ_1^I , ϕ_2^I are calculated using the biquadratic interpolation with 9 values on the cell center. A sketch of the implementation is shown in Fig. 3.

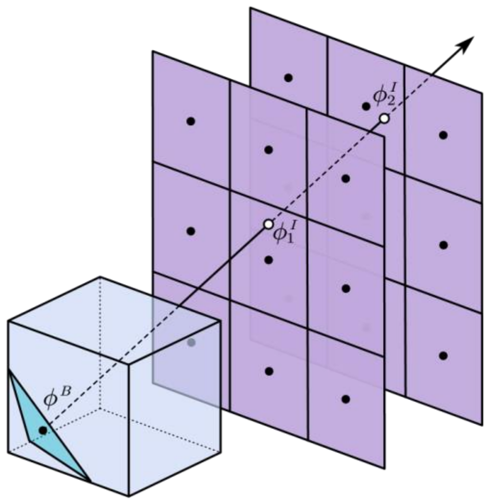

Fig. 3 A sketch of the 3-D implementation

NUMERICAL SETUP

Physical model

This paper simulates and studies flow past a single and two tandem surface-piercing cylinders under Froude number Fr equaling 1.3. The Froude number is defined as $Fr = U_0 / \sqrt{gD}$, where U_0 is the uniform inlet velocity, $g = 9.8067 m/s^2$ is the gravity acceleration, D is the diameter of the cylinder. Following previous experimental studies by Ageorges et al. (2019), D is set to 0.05m and the draught of the cylinder h is set to $h = 2.55D$. Then U_0 is set to $0.91 m/s$, correspondingly. The density ratio of water and air is set to $\rho_w / \rho_a = 1000/1 = 1000$ and the viscosity ratio of water and air is set to $\mu_w / \mu_a = 1.14\times10^{-3} / 1.79\times10^{-5} = 63.7$. The surface tension coefficient σ is set to 72.8mN/m. The location of the other cylinder is controlled by the gap length l between two cylinders. We have three different cases in this study $l / D = 2,3,5$.

Computational domain and mesh

The size of the computational domain is set to $-15D \leqslant x \leqslant 20D$ streamwise, $-15D \leqslant z \leqslant 15D$ cross-stream, and $-8D \leqslant y \leqslant 8D$ vertically. In the single-cylinder case, the origin is set to the center of the cylinder waterplane. In the tandem cylinder case, the origin is set to the center of the waterplane of the cylinder closer to the outlet. For the boundary conditions, a uniform inflow is set at the inlet and the Neumann boundary condition is applied for the outlet. A no-slip Dirichlet boundary condition is put on the surface of the circular cylinder using EBM, as discussed in the former section. A sketch of the computational model is shown in Fig. 4.

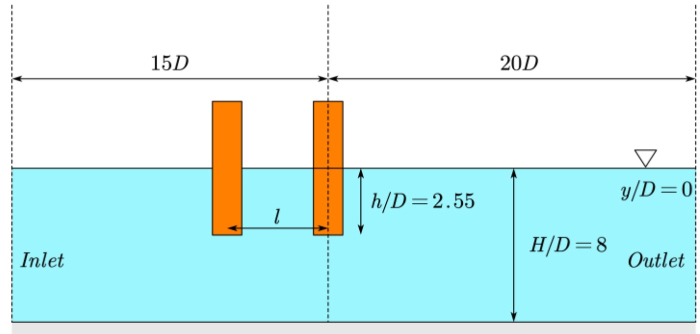

Fig. 4 A sketch of the computational model

Mesh convergence test and numerical validation

A mesh convergence test is performed at first using the single cylinder case with three different maximum refinement levels 8,9,10 (corresponding to $256^3, 512^3, 1024^3$ uniform meshes, respectively). The grid convergence index (GCI) introduced by Celik et al. (2008) is adopted and the bow wave height D_1 / D and the depression depth L_0 / D are the chosen flow parameters for quantification. The results are shown in Table 1. Parameter $\varepsilon_{21} = \psi_2 - \psi_1$ and $\varepsilon_{32} = \psi_3 - \psi_2$ are the absolute error where ψ is the value of the chosen flow parameters, the subscript 1,2,3 represents fine, medium, and coarse meshes, respectively. $R = \varepsilon_{21} / \varepsilon_{32}$ is the convergence ratio. As shown in Table 1, the absolute values of the convergence ratio for both parameters are low, indicating a converged trend. The numerical uncertainties of the fine mesh are $GCI_{21} = 1.186\%, 0.763\%$, indicating a low uncertainty for capturing the free surface characteristics. It is concluded that the fine mesh (maximum refinement level equal to 10) is sufficient for the numerical simulation and analysis.

Table 1 Mesh convergence study by GCI

Parameter	ε_{21}	ε_{32}	R	GCI_{21} (%)	GCI_{32} (%)
D_1 / D	-0.0148	-0.0538	0.2749	1.186	4.425
L_0 / D	0.0103	-0.0525	-0.1966	0.763	3.977

Then the numerical approaches are validated by a single cylinder case discussed in Chen et al. (2022). The free surface deformation on two different planes $z/D = 0$ and $z/D = 1$ simulated by the present approach is compared to the experimental results and DDES results. As shown in Fig. 5, the trend of the free surface deformation matches well with the experimental results and the previous numerical results.

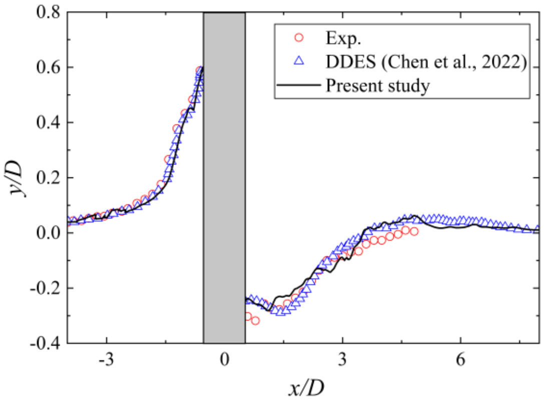

(a) $z / D = 0$

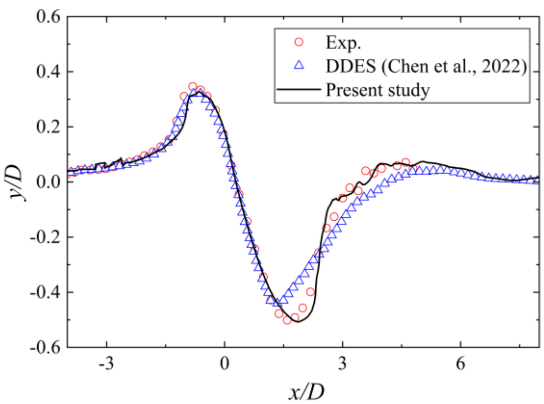

(b) $z / D = 1$

Fig. 5 Free surface deformation at $z / D = 0$ and $z / D = 1$

RESULTS AND DISCUSSIONS

Free surface deformation

Fig. 6 shows the time-averaged free surface deformation in the four cases. A typical wave run-up in front of the cylinder and a depression region behind the cylinder is observed in the single cylinder case. A wave crest is formed behind the depression region in the center, and the wave height decays along both sides. When a downstream cylinder is put into the flow field, the free surface deformation becomes complicated and shows many distinct characteristics. At $l / D = 2$, the free surface deformation behaves similarly to a single object. A vertical jet appears in front of the downstream cylinder with a steep slope observed between the cylinders, indicating active flow in this region. The depression region behind the cylinder is larger compared to the single cylinder case and the wave crest is also higher. This suggests a superposition effect of the wakes from the two circular cylinders. At $l / D = 3$, more free surface deformation is observed around the downstream cylinder. The free surface of the wake changes greatly near the *z*-direction centerline, with the wave crest in the center disappearing. This is distinct from the $l / D = 2$ case. However, the free surface away from the centerline is less influenced. At $l / D = 5$, the wake of the downstream cylinder separates from the front cylinder, suggesting a reduced tandem effect on the downstream cylinder. The wake of the front cylinder is more influenced by the bow wave of the downstream cylinder, leading to a reduced area and depth of the depression region. The wave height of the wake is even lower, showing a remarkable canceling effect which is contrary to the $l / D = 2$ case.

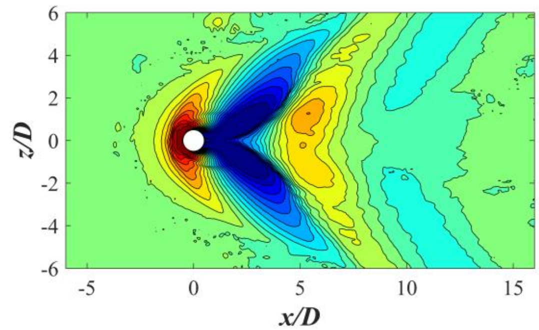

(a) Single cylinder

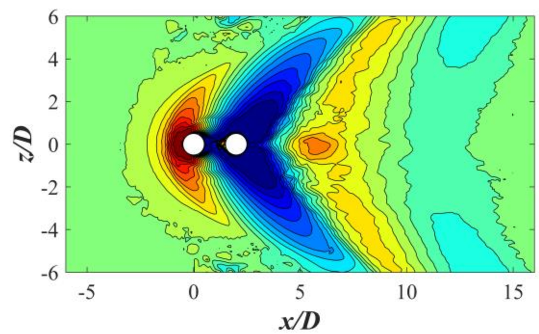

(b) $l / D = 2$

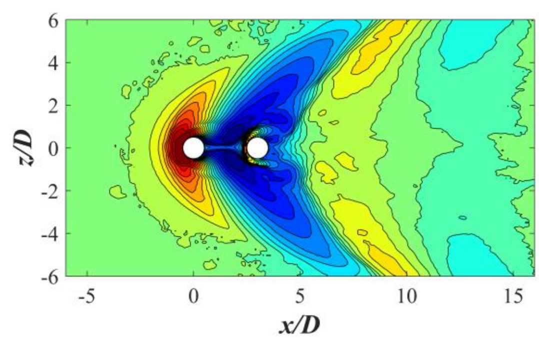

(c) $l / D = 3$

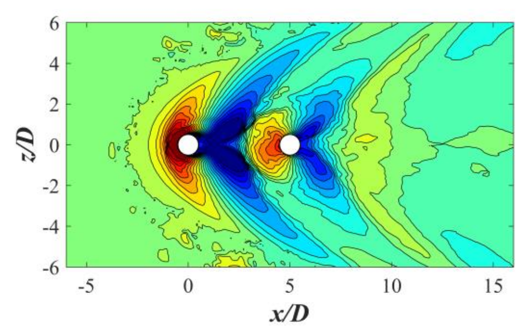

(d) $l / D = 5$

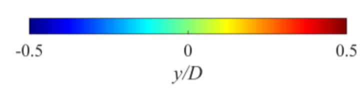

Fig. 6 Time-averaged free surface deformation

Fig. 7 further plots the time-averaged free surface deformation in the $z/D=0$ plane. The area between the two cylinders is hidden to better compare the characteristics of the bow wave and the wake region. It is observed that the bow wave height in front of the upstream cylinder is consistent in the four cases. It indicates that the flow in the front of the upstream cylinder is rarely affected by the downstream cylinder. The inflow of the downstream cylinder is masked by the upstream cylinder. Therefore, the bow wave reflection of the downstream cylinder is limited. In contrast, the wakes behind the downstream cylinder in the four cases vary a lot. At $l/D=2$, the wave crest behind the downstream cylinder is closer to the cylinder and higher than the single cylinder case. However, the wake decays quickly along the streamwise direction and disappears behind $x/D=5$. The wave crest is hardly seen at $l/D=3,5$. This conforms to the observation above that the wake shows a superposition regime at $l/D=2$ and shows a cancelling regime at $l/D=3,5$. Despite that, the depths of the depression region in the tandem cylinder flows are all smaller than that in the single cylinder case.

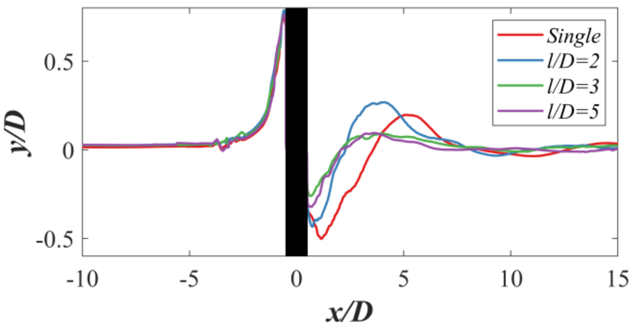

Fig. 7 Time-averaged free surface deformation on $z/D=0$

Velocity distribution

The tandem arrangement strongly influences the velocity distribution of the cylinder flow as well. Fig. 8 plots the velocity distribution at the central vertical plane in the four cases. The white line represents the time-averaged free surface. For the single cylinder case, flow separation is observed at both vertical ends of the cylinder. The separation in the air is larger than that in the water, due to the depression of the free surface. A larger vortex and backflow region is formed in the air subsequently. A high-speed region is observed under the wake, indicating a strong flow shearing in this region. The upwash flow generated from the free end also affects the wake flow. For $l/D=2$, the velocity distribution features change significantly compared to the single cylinder case. Due to the downstream cylinder's existence, the free-end flow separation from the upstream cylinder is attenuated. The shear layer in the water reattaches the free end of the downstream cylinder and the upwash flow is disappeared. On the contrary, the shear layer in the air doesn't reattach and a smaller vortex is formed in the gap. It is also observed that the high-speed region behind the downstream cylinder is larger, indicating a superposition regime and conforming to the observation of the free surface. For $l/D=3$, the flow characteristics in the gap region are more similar to that behind the single cylinder. The shear layer separated from the downstream cylinder is still mainly composed of shear layers from the upstream cylinder. The high-speed region behind the downstream cylinder is eliminated, indicating a canceling regime. The upwash flow is not observed in this case, but an upwash flow with a low speed is seen in the separation region. This phenomenon explains the reduction of the depression depth. For $l/D=5$, the influence of the downstream cylinder is reduced, with the flow separation and the upwash flow seen in the gap region. The shear layer independently generates from the free end of the downstream cylinder and forms a second upwash flow. By comparing the velocity distribution behind the upstream and the downstream cylinder, close relationships between the velocity distribution at $z/D=0$ and the free surface deformation are found. The steeper free surface is related to the high-speed flow beneath the free surface.

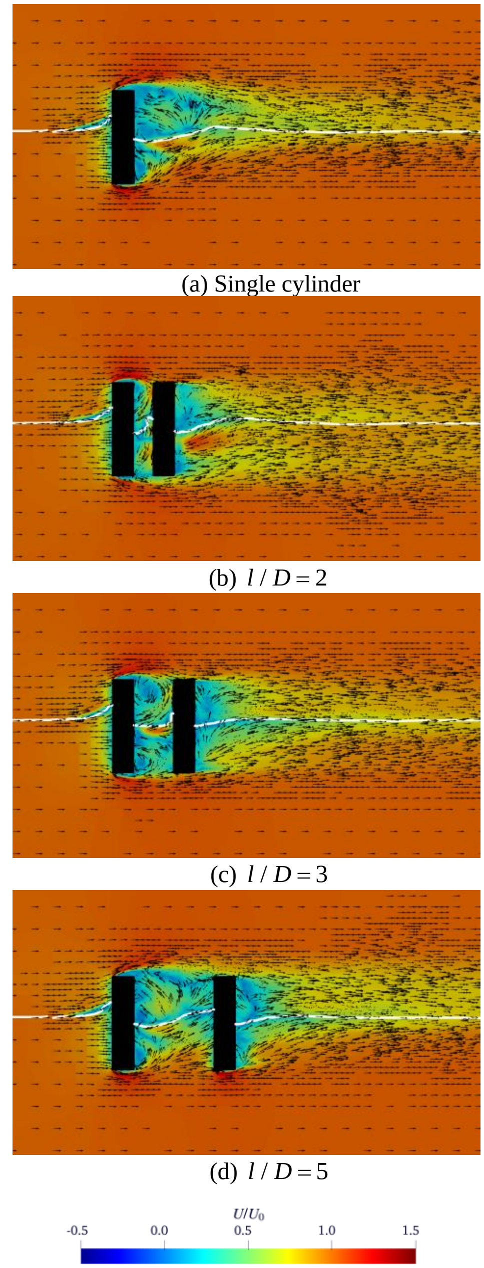

Fig. 8 Time-averaged velocity distribution at $z/D=0$

Vortex shedding

In this sub-section, we further discuss the combined influence of tandem arrangement, the free surface, and the free end on the flow features in the cylinder flow by investigating the vortex shedding characteristics. Fig. 9~11 show the vertical direction vortex shedding at different spanwise directions for the four cases. The vortex shedding feature shown in Fig.

9(b) which is in the middle of the single cylinder is close to the single-phase cylinder flow and plays the role of a standard pattern. Two symmetry shear layers develop and separate from the cylinder. The free surface and the free end significantly change the flow patterns. In Fig. 9(a), wider distributions of small vortexes are observed behind the circular cylinder and in the wake area. The vortex structures are closely related to the free surface deformation. Near the free end, the vortex shedding is suppressed a lot owing to the upwash flow discussed above, as shown in Fig. 9(c). The introduction of the tandem arrangement significantly changes the vortex shedding for all spanwise directions. In the middle for $l/D=2$ (Fig. 10(b)), the shear layer reattaches the downstream cylinder. The downstream cylinder plays a disturbing role in the vortex shedding, making the shedding wider and more unstable. However, near the free surface (Fig. 10(a)), the distribution width of the shedding is attenuated. This is because the vortexes reattach and separate from the downstream cylinder, and the downstream cylinder plays the role of vortex attraction. It is also observed that the vortexes are stronger due to the cylinder interaction. It is the origin of the high-speed region observed in Fig. 8(b) and further explains the superposition regime of the free surface deformation. Near the free end (Fig. 10(c)), vortex shedding is complete, varying greatly from the single case. This is due to the disappearance of the upwash flow discussed above. For all three spanwise directions, no flow separation and shear layers generated from the downstream cylinder are observed, indicating that the upstream cylinder masks the inlet flow. In this case, the two cylinders act like a whole elliptic cylinder. When the gap length increases to $l/D=3$ (Fig. 11), the shear layers separated from the middle fail to reattach the downstream cylinder and form complete vertical vortexes. The vortexes behind the downstream cylinder at $y/D=-1.5$ are still mainly composed of vortexes from the upstream, except for a weak pair of vortexes seen near the center behind the downstream cylinder. However, the flow separation of the upstream cylinder near the free surface is attenuated compared to the single case. The active free surface deformation in the gap produces a vortex region in front of the downstream cylinder. Two shear layers are observed behind the downstream cylinder and form the vortex shedding near the centerline. The vortexes from the upstream move to the two sides. Near the free end, the vortexes generated by the upstream cylinder attach to the center of the downstream cylinder and disappear. The vortex shedding in the wake region is generated by the downstream cylinder. It indicates that a slight upwash flow forms in the gap and the inflow resumes near the free end of the downstream cylinder. For $l/D=5$, two separate vortex shedding regions are observed behind the two cylinders (Fig. 12(b)). The separation point and the form of the downstream vortex differ from the single case, which is mainly influenced by the extrusion effect of the upstream vortexes. A similar effect is observed near the free surface. However, the vortex shedding for $l/D=5$ is very close to the single case, conforming to the two upwash flows observed in Fig. 8(d). For all three tandem cases, the vortex density and distribution width are larger than that in the single case. It illustrates the additional flow instability and energy dissipation are caused by the downstream cylinder. This also explains the quick decay of the wake at $l/D=2$ and the cancelling regime at $l/D=3,5$.

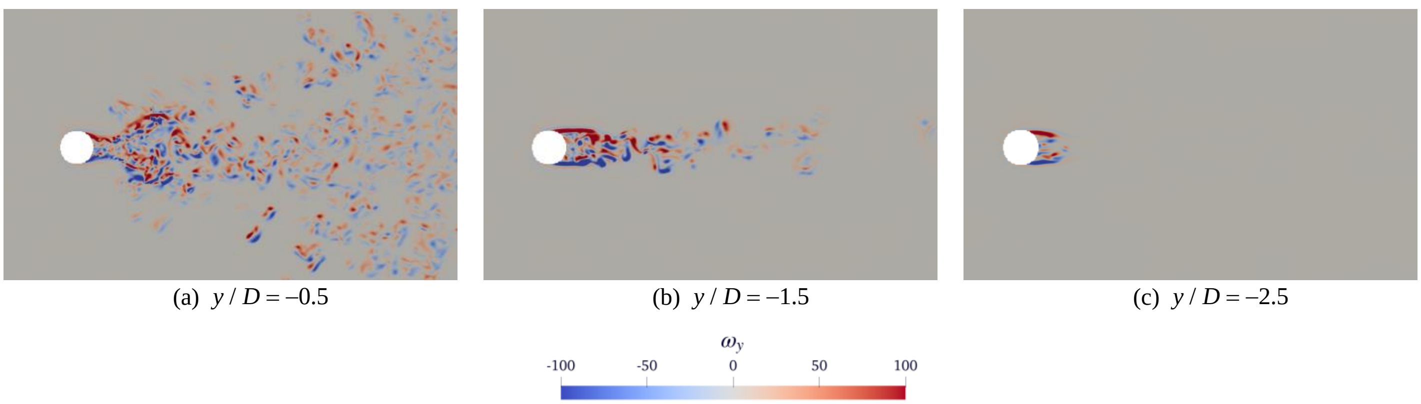

(a) $y/D=-0.5$ (b) $y/D=-1.5$ (c) $y/D=-2.5$

Fig. 9 Instantaneous vorticity distributions at different spanwise directions for the single case

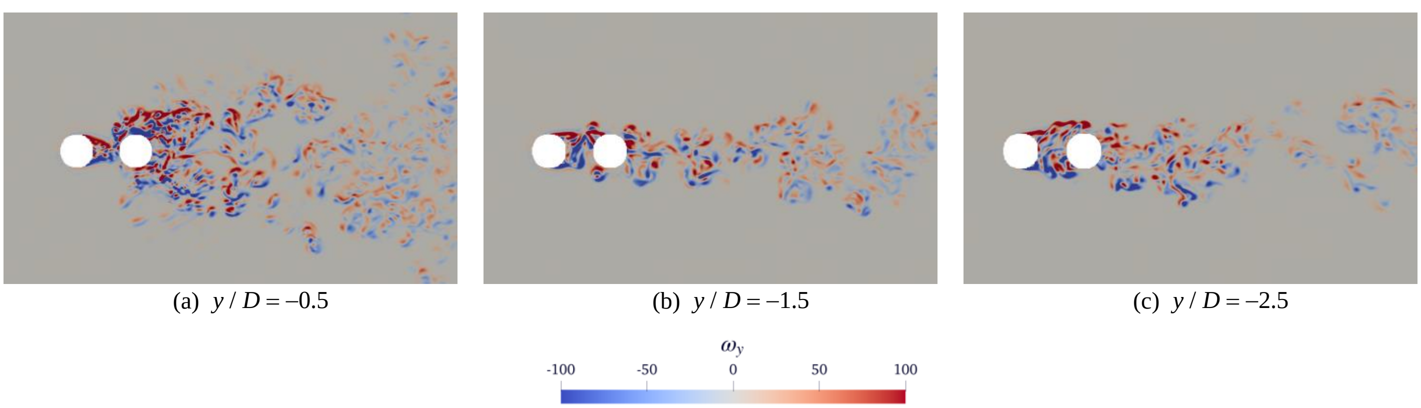

(a) $y/D=-0.5$ (b) $y/D=-1.5$ (c) $y/D=-2.5$

Fig. 10 Instantaneous vorticity distributions at different spanwise directions for $l/D=2$

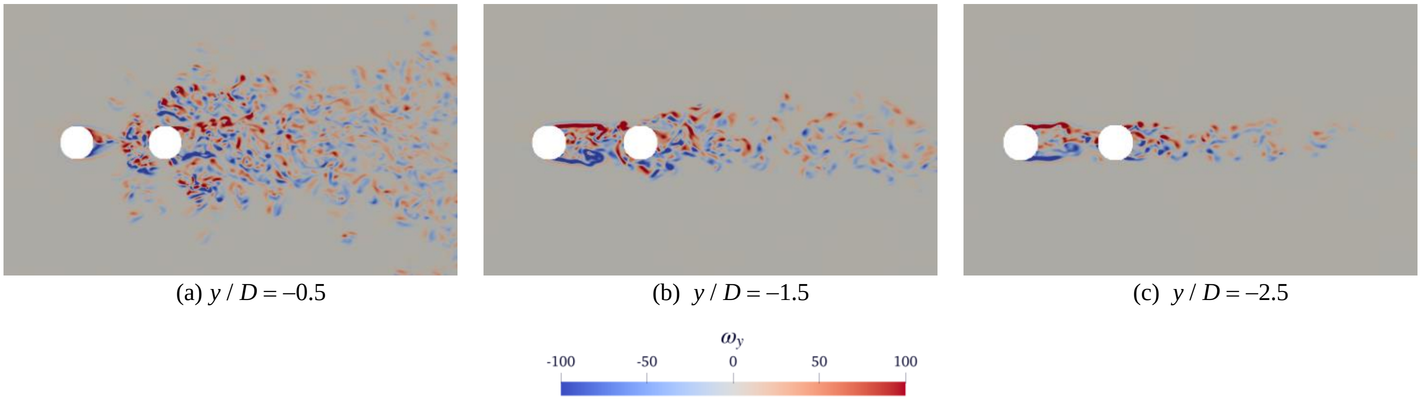

Fig. 11 Instantaneous vorticity distributions at different spanwise directions for $l/D=3$

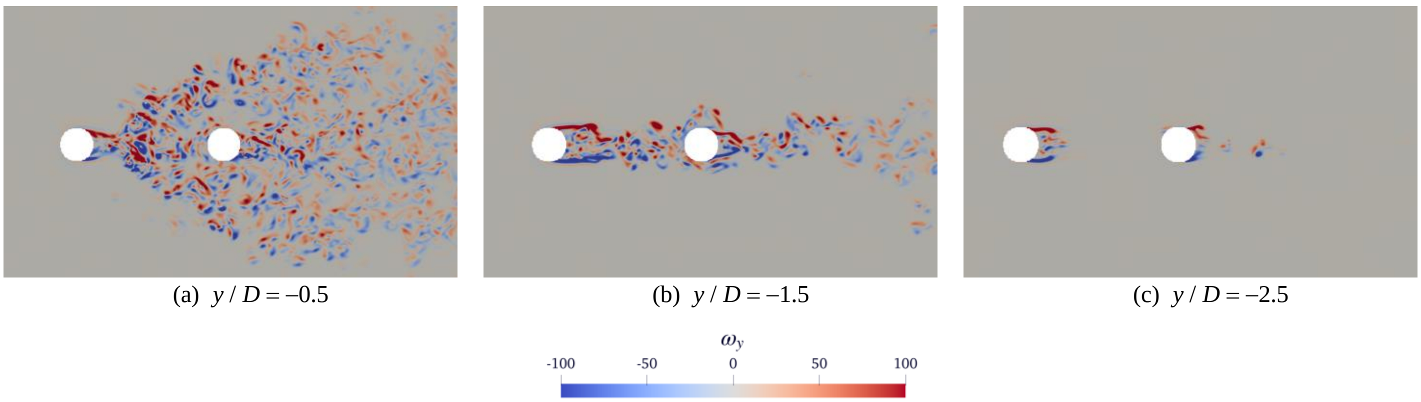

Fig. 12 Instantaneous vorticity distributions at different spanwise directions for $l/D=5$

CONCLUSIONS

In this study, the flows past two tandem surface-piercing finite circular cylinders with various gap lengths are investigated numerically based on adaptive Cartesian meshes. The tandem impact on the free surface deformation, the velocity distribution, and the vortex shedding are discussed, respectively. The main conclusions are as follows:

(1) Tandem impact on the free surface deformation: The wake region is much more influenced by the tandem arrangement, while the free surface deformations in the bow wave regions remain the same for different cases. For $l/D=2$, the wake shows a superposition regime; For $l/D=3,5$, the wake shows a canceling regime.

(2) Tandem impact on the velocity distribution: The velocity distributions in the gap and the wake are closely related to the gap length l/D. Distinct flow patterns including the flow separation at the free end, the circulation flow in the gap, and the upwash flow are identified for the three cases.

(3) Tandem impact on the vortex shedding: The features of the vortex shedding in the cylinder wake change significantly due to the tandem arrangement. The interactions between the vortexes generated by the two cylinders are distinct with different gap length ratios. The behaviors of tandem impact also vary in different spanwise directions. The tandem arrangement, the free surface, and the free end show combined effects on the vortex shedding, with many distinct patterns identified.

ACKNOWLEDGMENT

This work is supported by the National Natural Science Foundation of China (52131102), to which the authors are most grateful.

REFERENCES

Ageorges, V, Peixinho, J, and Perret, G (2019). "Flow and air-entrainment around partially submerged vertical cylinders," *Phys Rev Fluids*, 4(6), 064801.

Ageorges, V, Peixinho, J, Perret, G, Lartigue, G, and Moureau, V (2021). "Experiments and Simulations of Free-Surface Flow behind a Finite Height Rigid Vertical Cylinder," *Fluids*, 6(10), 367.

Carmo, BS, and Meneghini, JR (2006). "Numerical investigation of the flow around two circular cylinders in tandem," *J Fluids Struct*, 22(6), 979–988.

Celik, IB, Ghia, U, Roache, PJ, and Freitas, CJ (2008). "Procedure for estimation and reporting of uncertainty due to discretization in CFD applications," *J FLUIDS Eng-Trans ASME*, 130(7), 078001.

Chaplin, JR, and Teigen, P (2003). "Steady flow past a vertical surface-piercing circular cylinder," *J Fluids Struct*, 18(3), 271–285.

Chen, S, Zhao, W, and Wan, D (2022). "Turbulent structures and characteristics of flows past a vertical surface-piercing finite circular cylinder," *Phys Fluids*, 34(1), 015115.

Hay, A (1947). "Flow about semi-submerged cylinders of finite length," *Princet Univ Princet NJ*,.

Hilo, AK, Hong, J-W, Kim, K-S, Ahn, B-K, Lim, G-S, and Shin, S (2022). "Experimental study on the flow patterns and acoustic characteristics of surface piercing cylinders," *Ocean Eng*, 259, 111895.

Kawamura, T, Mayer, S, Garapon, A, and Sørensen, L (2001). "Large Eddy Simulation of a Flow Past a Free Surface Piercing Circular Cylinder," *J Fluids Eng*, 124(1), 91–101.

Keough, SJ, Ooi, A, Philip, J, and Monty, JP (2024). "Characterisation of flow regimes in the bow wave of a surface piercing cylinder," *Appl Ocean Res*, 145, 103936.

Kitagawa, T, and Ohta, H (2008). "Numerical investigation on flow around circular cylinders in tandem arrangement at a subcritical Reynolds number," *J Fluids Struct*, 24(5), 680–699.

Koo, B, Yang, J, Yeon, SM, and Stern, F (2014). "Reynolds and froude number effect on the flow past an interface-piercing circular cylinder," *Int J Nav Archit Ocean Eng*, 6(3), 529–561.

Schwartz, P, Barad, M, Colella, P, and Ligocki, T (2006). "A Cartesian grid embedded boundary method for the heat equation and Poisson's equation in three dimensions," *J Comput Phys*, 211(2), 531–550.

Suh, J, Yang, J, and Stern, F (2011). "The effect of air–water interface on the vortex shedding from a vertical circular cylinder," *J Fluids Struct*, 27(1), 1–22.

Zdravkovich, MM (1987). "The effects of interference between circular cylinders in cross flow," *J Fluids Struct*, 1(2), 239–261.